

Benchmarking variational quantum eigensolvers for the square-octagon-lattice Kitaev model

Andy C. Y. Li,¹ M. Sohaib Alam,² Thomas Iadecola,^{3,4} Ammar Jahin,⁵ Doga Murat Kurkcuoglu,¹ Richard Li,⁶ Peter P. Orth,^{3,4} A. Barış Özgüler,¹ Gabriel N. Perdue,¹ and Norm M. Tubman⁷

¹*Fermi National Accelerator Laboratory, Batavia, IL, 60510, USA*

²*Rigetti Computing, Berkeley, CA, 94701, USA*

³*Department of Physics and Astronomy, Iowa State University, Ames, Iowa 50011, USA*

⁴*Ames Laboratory, Ames, Iowa 50011, USA*

⁵*Department of Physics, University of Florida, 2001 Museum Rd, Gainesville, FL 32611, USA*

⁶*Department of Physics, Yale University, New Haven, Connecticut 06520, USA*

⁷*Quantum Artificial Intelligence Lab. (QuAIL), Exploration Technology Directorate, NASA Ames Research Center, Moffett Field, CA 94035, USA*

(Dated: September 9, 2021)

Quantum spin systems may offer the first opportunities for beyond-classical quantum computations of scientific interest. While general quantum simulation algorithms likely require error-corrected qubits, there may be applications of scientific interest prior to the practical implementation of quantum error correction. The variational quantum eigensolver (VQE) is a promising approach to find energy eigenvalues on noisy quantum computers. Lattice models are of broad interest for use on near-term quantum hardware due to the sparsity of the number of Hamiltonian terms and the possibility of matching the lattice geometry to the hardware geometry. Here, we consider the Kitaev spin model on a hardware-native square-octagon qubit connectivity map, and examine the possibility of efficiently probing its rich phase diagram with VQE approaches. By benchmarking different choices of variational ansatz states and classical optimizers, we illustrate the advantage of a mixed optimization approach using the Hamiltonian variational ansatz (HVA). We further demonstrate the implementation of an HVA circuit on Rigetti’s Aspen-9 chip with error mitigation.

I. INTRODUCTION

In the context of quantum computation there is reason to believe the quantum simulation of spin systems may offer early results in the search for beyond classical computations of real scientific interest [1]. Although beyond-classical calculations that offer truly new insights into scientific problems will likely require quantum error correction (QEC) [2, 3], it may be possible to find approachable questions of scientific interest even before the advent of full QEC if we carefully pair the computing hardware and problem. Lattice models are a natural class of systems to consider in this regard, and they also tend to have sparse Hamiltonian representations that require fewer quantum resources than other Hamiltonian models [4]. In this work, we consider a spin model [5, 6] that maps naturally onto the square-octagon qubit connectivity of a superconducting quantum processor and perform an open study of the most efficient ways of finding the ground state of this system using variational quantum algorithms based on parameterized quantum circuits.

The near-term, so-called “Noisy Intermediate Scale Quantum” (NISQ) [7–9] computing era is defined by the conditions imposed by noisy quantum hardware. Decoherence errors mandate the use of “shallow” quantum circuit programs, i.e., quantum circuits with a small number of consecutive operations on the qubit register array. Quantum noise also currently limits the effective “width” of a circuit, which is governed by the total number of qubits deployed. A wide circuit consists of more quantum gates than a narrow circuit, and thus the gate error

rates effectively limit how wide a circuit could be before the result becomes no longer useful with the decreasing circuit fidelity.

The variational quantum eigensolver (VQE) [10–17] is an algorithm that seeks to implement low-depth variational ansatz circuits to find eigenstates of complex many-body Hamiltonians. Different approaches to VQE entail different choices of ansatz circuits, which take into account different figures of merit. These can include reducing the circuit depth, increasing the accuracy or wavefunction fidelity, or minimizing the number of variational parameters. To match these varied goals, there are many different approaches which include hardware efficient ansatzes (HEA) [13], adaptive ansatzes [14, 16], and ansatzes inspired by classical simulations [13, 16, 18]. One particular ansatz of interest is the Hamiltonian variational ansatz (HVA) [19]. This ansatz draws from ideas expressed by the quantum approximate optimization algorithm (QAOA) and adiabatic quantum computation [20, 21]. Recent work [22] suggests the HVA may be less prone to problems with “barren plateaus” [23] and therefore easier to optimize than the HEA (see, however, Ref. [24]).

Kitaev spin models [5, 25, 26], which are a family of frustrated quantum spin models with bond-dependent interactions, provide an intriguing testbed for NISQ quantum simulation. Kitaev models can be defined on arbitrary trivalent graphs and are appealing due to their exact solvability via a mapping to free Majorana fermions [5]. Despite their simplicity, they yield a rich variety of phases, including gapped \mathbb{Z}_2 and gapless $U(1)$

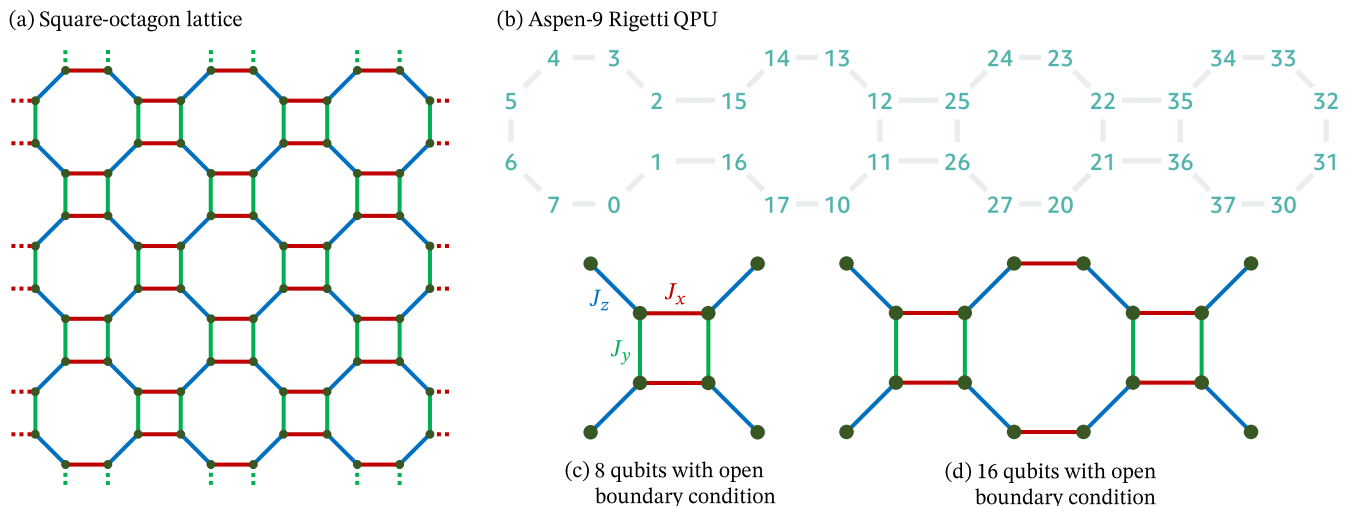


FIG. 1. **Lattice geometry.** A square-octagon lattice with the Kitaev couplings is shown in (a). The Aspen-9 QPU is arranged with a square-octagon connectivity shown in (b). Note that qubits 1 and 2, and qubits 15 and 16 are not connected due to a hardware issue. The Aspen-9 geometry allows us to pick part of it to simulate a square-octagon-lattice Kitaev model with open boundary condition, for example, the 8-qubit lattice in (c) and the 16-qubit lattice in (d). The J_x (red), J_y (green) and J_z (blue) couplings are assigned to each of the linkage.

spin liquids [27]. In a magnetic field, Kitaev models support non-Abelian Ising anyons [5], which (in addition to the aforementioned \mathbb{Z}_2 spin-liquid phase) makes them a promising platform for topological quantum computation [28–30]. Kitaev-like models are predicted to arise in spin-orbit-coupled Mott insulators [31], and a plethora of materials candidates exist [26]. Putative signatures of spin-liquid physics have been observed in neutron scattering [32, 33] and thermal transport measurements [34, 35].

In realistic systems, the desired “Kitaev interactions” compete with more mundane (e.g. Heisenberg) interactions and external magnetic fields, all of which spoil the Kitaev model’s exact solvability and often favor magnetically ordered ground states. One therefore must resort to numerical methods [36–50], such as exact diagonalization (ED), tensor-network techniques like the density-matrix renormalization group (DMRG) [51–53], and Monte Carlo [54, 55], to study the ground-state phase diagram. Thus, Kitaev models provide a useful benchmark for near-term quantum algorithms for the study of interacting quantum systems.

In this paper, we focus on the Kitaev model on the square-octagon lattice [6, 56], which maps natively with minimal compilation overhead onto Rigetti’s Aspen architecture featuring 32 transmons with a square-octagon topology [57–59]. This native mapping makes the quantum simulation of the square-octagon Kitaev model a potential NISQ application of the Aspen-9 quantum processing unit (QPU) to carry out beyond-classical calculations without full QEC. We will benchmark the variational ansatzes and optimization algorithms to determine the ground state of the Kitaev model. Supported by the result of classical simulations, we will illustrate a mixed optimization approach using both a local optimizer and

a non-local optimizer started with multiple initial values. Together with an experimental test run of a classically optimized VQE circuit on the QPU, this investigation provides insights into the appropriate VQE approach for further VQE experiments with a system size beyond the capability of classical computation.

This paper is organized as follows. In section II A, we review the Kitaev model on the square-octagon lattice and its phase diagram in the presence of a magnetic field. This is followed by a review of VQE approaches in section II B. We discuss our methodology for investigating the circuit ansatzes (section III B) and optimizers (section III C), and for implementing the classically optimized circuits on Aspen-9 with noise mitigation (section III D). The results of the investigation are then discussed in section IV.

II. BACKGROUND

A. Square-octagon-lattice Kitaev model

The ferromagnetic Kitaev model on the square-octagon lattice has the Hamiltonian,

$$H_K = -J_x \sum_{x\text{-bonds}} X_i X_j - J_y \sum_{y\text{-bonds}} Y_i Y_j - J_z \sum_{z\text{-bonds}} Z_i Z_j, \quad (2.1)$$

where $J_{x,y,z} > 0$ and we partition the nearest-neighbor bonds of the lattice into x , y , and z sets depending on their orientation (see Fig. 1(a)), and $\{X_i, Y_i, Z_i\}$ are the Pauli matrices for site i . Like the original honeycomb-lattice version, the Kitaev model H_K on the square-

octagon lattice is exactly solvable by mapping to free fermions [6]. To move beyond the exactly solvable limit and explore the rich phase diagram emerging in finite magnetic field (see Fig. 2, we consider the model

$$H = H_K + \sum_i (h_x X_i + h_y Y_i + h_z Z_i), \quad (2.2)$$

where $\vec{h} = (h_x, h_y, h_z)$ is the magnetic field. This Hamiltonian and variants thereof have been studied in Refs. [6, 56, 60–62] using a variety of methods, and the general features of its phase diagram are well-understood.

At zero field, the model features two gapped \mathbb{Z}_2 spin-liquid phases, which we dub TC_z and TC_{xy} . The TC_z phase can be understood perturbatively in the limit $J_z^2 \gg J_x^2 + J_y^2$, where an effective Hamiltonian equivalent to the well-known toric code [63] emerges [6, 56]. The TC_{xy} phase can be understood in the opposite limit $J_x^2 + J_y^2 \gg J_z^2$, where perturbation theory yields [56] a Hamiltonian equivalent to the so-called Wen-plaquette model [64], which is in turn equivalent to the toric code [65, 66]. In both TC phases, the model has \mathbb{Z}_2 topological order and supports Abelian anyonic excitations with nontrivial mutual statistics; nevertheless, the phases are distinct [56, 62]. A critical line separating these two gapped phases appears at $J_z^2 = J_x^2 + J_y^2$.

At small but finite field, the TC phases persist [61], as is expected due to the gapped nature of these phases. Provided that none of $h_{x,y,z} = 0$, the gapless line at $J_z^2 = J_x^2 + J_y^2$ gives way to a gapped phase with non-Abelian Majorana excitations [6]. At large field, the system enters a trivial spin-polarized paramagnetic phase. The phase diagram of the square-octagon Kitaev model in a field has been studied in Refs. [6, 60, 61], but a detailed understanding of the location of all transitions is lacking. A schematic of the phase diagram for $J_x = J_y = J_\perp$ in a [111]-oriented field $\vec{h} = h_{[111]}(1, 1, 1)/\sqrt{3}$ is shown in Fig. 2.

In the following, we focus on a number of representative points in the phase diagram, which are highlighted in Fig. 2 and defined in Table I. The table also includes the exact ground state energies for these parameters that are obtained using ED, which we will use to benchmark our VQE results. We consider lattices with open boundary condition shown in Fig. 1(c,d) for the benchmarks.

B. VQE

VQE algorithms prepare the eigenstates of the system Hamiltonian H by optimizing the cost function associated with a trial state $|\psi(\vec{\theta})\rangle$, which is prepared by a parameterized circuit ansatz $U(\vec{\theta})$ such that $|\psi(\vec{\theta})\rangle = U(\vec{\theta})|0\rangle$ [11, 13]. To prepare the ground state, the VQE algorithm minimizes, using a classical optimizer, the energy of the trial state, i.e.,

$$E(\vec{\theta}) = \langle \psi(\vec{\theta}) | H | \psi(\vec{\theta}) \rangle. \quad (2.3)$$

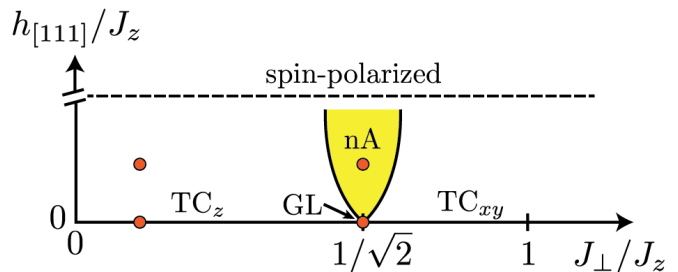


FIG. 2. **Phase Diagram.** Schematic phase diagram of the Kitaev model (2.2) on the square-octagon lattice as a function of spin exchange anisotropy J_\perp/J_z with $J_\perp \equiv J_x = J_y$ and magnetic field in [111] direction $h_{[111]}$. It includes gapped toric code phases (TC_z , TC_{xy}) that are stable with respect to small fields, the gapless line (GL) at $J_\perp/J_z = 1/\sqrt{2}$ and a phase with non-Abelian (nA) Majorana excitations that emerges in field above the gapless line. At large magnetic fields the system enters a spin-polarized paramagnetic phase. The red circles denote the different, representative model parameter points that are studied in our benchmark simulations.

TABLE I. **Definition of studied model parameter values.** This table contains the model parameter values that are used in our benchmark simulations below. They correspond to positions in the phase diagram in the toric code phase without magnetic field (TC_z) and with a magnetic field ($\text{TC}_z + h$), on the gapless line (GL) and above the gapless line in magnetic field ($\text{GL} + h$). The ground-state energy E_g is determined by ED for the 8-qubit lattice ($N = 8$) and the 16-qubit lattice ($N = 16$) with open boundary conditions shown in Fig. 1(c) and (d).

Label	J_x	J_y	J_z	h_x	h_y	h_z	$E_g(N = 8)$	$E_g(N = 16)$
TC_z	0.1	0.1	1	0	0	0	-4.0100	-8.0250
$\text{TC}_z + h$	0.1	0.1	1	$\frac{0.05}{\sqrt{3}}$	$\frac{0.05}{\sqrt{3}}$	$\frac{0.05}{\sqrt{3}}$	-4.2476	-8.5002
GL	$\frac{1}{\sqrt{2}}$	$\frac{1}{\sqrt{2}}$	1	0	0	0	-4.4721	-9.3002
$\text{GL} + h$	$\frac{1}{\sqrt{2}}$	$\frac{1}{\sqrt{2}}$	1	$\frac{0.05}{\sqrt{3}}$	$\frac{0.05}{\sqrt{3}}$	$\frac{0.05}{\sqrt{3}}$	-4.7011	-9.7008

The cost function is measured on the QPU, and the result fed into the classical optimizer, making the VQE a hybrid quantum-classical approach. Several different approaches are possible for calculating excited states [10, 12, 67, 68]. One approach is to minimize a modified cost function including the overlaps with the lower-energy eigenstates determined in the previous iterations [69, 70].

Similar to other variational algorithms, the output of VQE only approximates the eigenstates of H , and the quality of the solution depends on the choice of ansatz. The true ground state cannot be expressed by the trial state $|\vec{\theta}\rangle$ if an inappropriate ansatz is chosen, resulting in an approximated energy much higher than the true ground-state energy. The success of VQE algorithms hence strongly depends on the circuit ansatz. Optimizing a generic HEA is a challenging task for several reasons, for example, the Barren plateaus [23] and the sensitivity to the optimizer meta-parameters [71]. The challenge

of optimization grows even bigger with the rapidly increasing number of variational parameters with the system size. The HVA, built using rotations generated by Hamiltonian terms, has been suggested to be a more efficient option than HEA in certain cases [22], as has been observed in several numerical simulations [71–73]. Later in this paper, we will compare the effectiveness of these two ansatzes in preparing the ground state of the square-octagon Kitaev model with 8 and 16 qubits.

The choice of classical optimization algorithm plays an important role in VQE implementations as well. Picking an inappropriate optimizer results in a slow convergence rate (and thus a longer QPU runtime), if it ever converges to a sufficiently good minimum at all [71, 74–76]. We will also benchmark the efficiency of a few optimizers using the Kitaev model to provide some insights into the VQE optimization strategy.

III. METHODOLOGY

A. Overview of approach

In the following sections we review our theoretical and experimental approaches to studying VQE simulations of the Kitaev model. Our study first aims, via classical simulations, to understand the modeling requirements for obtaining different phases of the Kitaev model with various ansatzes and optimizers, and then tests these approaches on present-day quantum hardware.

B. VQE Ansatz

We construct the HVA using the Kitaev couplings J_x , J_y and J_z in Eq. (2.1), and the magnetic fields h_x , h_y and h_z in the Eq. (2.2). The HVA represented by the unitary matrix $U(\vec{\theta})$ has L layers such that

$$U(\vec{\theta}) = U_{\text{HVA}}(\vec{\theta}_L)U_{\text{HVA}}(\vec{\theta}_{L-1}) \cdots U_{\text{HVA}}(\vec{\theta}_1). \quad (3.1)$$

Each layer $U_{\text{HVA}}(\vec{\theta}_\ell)$ consists of the exponentiation of the Kitaev couplings and the magnetic fields multiplied by the parameters $\vec{\theta}_\ell$ such that

$$\begin{aligned} U_{\text{HVA}}(\vec{\theta}_\ell) = & e^{-i\theta_{\ell,6} \sum_i Z_i} e^{-i\theta_{\ell,5} \sum_{z\text{-bonds}} Z_i Z_j} \\ & \times e^{-i\theta_{\ell,4} \sum_i Y_i} e^{-i\theta_{\ell,3} \sum_{y\text{-bonds}} Y_i Y_j} \\ & \times e^{-i\theta_{\ell,2} \sum_i X_i} e^{-i\theta_{\ell,1} \sum_{x\text{-bonds}} X_i X_j}. \end{aligned} \quad (3.2)$$

The two-qubit gate count N_b of each HVA layer scales linearly with the number N of qubits. (For an infinite square-octagon lattice, $N_b = \frac{3}{2}N$.) The Aspen-9 connectivity shown in Fig. 1(b) is natively the square-octagon lattice. One HVA layer can then be executed with $N_b \sim N$ CPHASE gates supported natively by Aspen-9 [59]. If we execute the circuit on a QPU with a different two-dimensional connectivity, an overhead of

$\mathcal{O}(N)$ SWAP gates will be required for implementing the HVA. Although this overhead does not change the overall gate complexity $\mathcal{O}(N)$ of the HVA implementation, it can still be quite demanding for NISQ devices. Using the Aspen-9 QPU with the native connectivity provides a significant advantage in the near term.

There are six parameters for each HVA layer, independent of the system size N . This makes the optimization of the HVA straightforward to analyze with increasing system size. We can make a rough estimate of how many times the cost function has to be evaluated based on the results on smaller lattices with a similar number of layers. Nonetheless, if the ground state of a larger system exhibits longer-range entanglement, more layers will typically be needed to achieve the same degree of accuracy as in a smaller system. Hence, the required number of layers and the total number of parameters depend on the system size, and usually can only be determined by experiments. This makes the prediction nontrivial especially when we consider small lattices in Fig. 1 with noticeable finite-size effects.

Other than HVA, we consider the HEA which is widely used in NISQ applications [13, 77, 78]. The general principle of the HEA is to construct circuit ansatzes using the native gates supported by the QPU, and hence different specific forms of the HEA are constructed targeting different QPUs. For Aspen-9, the native gate set consists of the XY gate [58], the CPHASE and CZ gates [59] as well as the single-qubit gates $R_Z(\theta)$, $R_X(k\pi/2)$ with $k = \pm 1, 2$. Moreover, the Quil programming language [79] and its accompanying optimizing compiler Quil-C [80] on the Rigetti stack [81] admits parametric compilation, which allows for the ansatz to be compiled only once, so that the numerical values of the ansatz parameters are only updated at runtime, without the need of incurring the compilation overhead at every step of the optimization process. This allows for faster execution times and feedback loops between the quantum and classical processor in the hybrid computation.

Roughly speaking, a HEA usually consists of layers of parameterized single-qubit rotations and two-qubit gates to create entanglement between qubits. Adopting this idea with respect to the Aspen-9 native gate set and its connectivity, we consider two ansatzes, namely the HEA-CZ using CZ gates and single-qubit rotation gates, and the HEA-XY using XY gates and single-qubit rotation gates. Here, we focus ourselves on the native two-qubit gates (CZ and XY) and slightly relax the native restriction on the single-qubit gates since the single-qubit gates have a much lower error rate than that of the two-qubit gates. The unitary representation U of an N -layer HEA is given by

$$U(\vec{\theta}) = U_{\text{HEA}}(\vec{\theta}_L) \cdots U_{\text{HEA}}(\vec{\theta}_1) U_0(\vec{\theta}_0). \quad (3.3)$$

Here, the layer U_0 preparing each qubit in an arbitrary unentangled state is given by

$$U_0(\vec{\theta}_0) = \prod_i R_{Z,i}(\theta_{0;1,i}) R_{X,i}(\theta_{0;0,i}). \quad (3.4)$$

TABLE II. **Classical optimization algorithms.** The different types of optimizers tested for the VQE algorithm. These include gradient-free, gradient-based, and non-local optimizers, and a genetic algorithm.

Optimizer	Gradient-free	Genetic	Local
BFGS	×	×	✓
BOBYQA [82]	✓	×	✓
CMA-ES [83]	✓	✓	×
Dual Annealing [84]	✓	×	×
SPSA [85]	×	×	✓

Note that an arbitrary single-qubit rotation is represented by the gate sequence $R_Z R_X R_Z$. The rightmost R_Z can be omitted here since the qubits are initialized in the 0-state and $R_Z|0\rangle$ just gives an irrelevant global phase. The other layers U_{HEA} then entangle the qubits using the two-qubit gates. For HEA-CZ, we have

$$U_{\text{HEA}}(\vec{\theta}_\ell) = \prod_{j,k \in G} R_{Z,j}(\theta_{\ell;4,(j,k)}) R_{Z,k}(\theta_{\ell;3,(j,k)}) \\ \times R_{X,j}(\theta_{\ell;2,(j,k)}) R_{X,k}(\theta_{\ell;1,(j,k)}) CZ_{j,k},$$

where G represents the hardware-native connectivity. Similarly, for HEA-XY, we have

$$U_{\text{HEA}}(\vec{\theta}_\ell) \\ = \prod_{j,k \in G} R_{Z,j}(\theta_{\ell;6,(j,k)}) R_{Z,k}(\theta_{\ell;5,(j,k)}) \\ \times R_{X,j}(\theta_{\ell;4,(j,k)}) R_{X,k}(\theta_{\ell;3,(j,k)}) \\ \times R_{Z,j}(\theta_{\ell;2,(j,k)}) R_{Z,k}(\theta_{\ell;1,(j,k)}) XY_{j,k}(\theta_{\ell;0,(j,k)}).$$

Once again, the sequence $R_Z R_X R_Z$ represents an arbitrary single-qubit rotation. For HEA-CZ, since R_z commutes with CZ, the first R_z can be combined with the last R_z in the previous layer. $U_{\text{HEA}}(\vec{\theta}_\ell)$ thus requires two less single-qubit gates for HEA-CZ than for HEA-XY.

In the present case, with the native connectivity being the same as the lattice geometry, the number of two-qubits gates of the HEA scales as N , which is the same as for the HVA, as expected. On the other hand, the number of parameters per layer also scales linearly with N , in contrast to the constant scaling of the HVA. The much larger number of parameters makes the HEA more expressive especially when a small number of layers is used. However, this also makes the HEA hard to scale up since optimizing a large number of parameters is challenging for non-convex cost functions.

C. Optimizers

The cost function associated with VQE algorithms is in general non-convex with many local extrema. Similar to optimizing other classical non-convex cost functions,

it is typically hard to decide an efficient optimizer *a priori* [86]. To make our benchmark less dependent on a specific choice of the optimizer, we will test the list of optimizers shown in Table II. This list consists of a few well-known gradient-free algorithms (BOBYQA, CMA-ES, dual annealing), gradient-based optimizers (SPSA, BFGS), non-local optimizers (CMA-ES, dual annealing), and a genetic algorithm (CMA-ES). Even though this is far from a comprehensive list, we can gain insight into how different types of optimizers work for our specific VQE cost function.

We compute the gradients needed for the gradient-based optimizers by finite-difference methods, which require an additional measurement of the cost function using the QPU for each gradient $\frac{\partial \langle E(\vec{\theta}) \rangle}{\partial \theta_j}$. This makes the cost of running these gradient-based optimizers larger than for the gradient-free algorithms, and thus makes them not the best choice currently given the limited QPU's clock rate. More efficient quantum algorithms to evaluate gradients have attracted great interest recently [87–89]. These algorithms usually require ancilla qubits and/or extra gate operations, and thus are challenging to implement on NISQ devices. However, once QPUs with better gate fidelities and coherence properties are available, further studies will be required to revisit these results and strike a balance between quantum resource requirements and optimization efficiency.

D. Experiment and noise mitigation

We ran the HVA with 1 layer on an 8-qubit sub-lattice of Rigetti's Aspen-9 QPU. We perform randomized compilation [90] to twirl the physical error channels into stochastic errors. In the HVA, the exponential of every 2-body term can be compiled using 2 native CZs. Before each CZ gate, we apply random Pauli operators $\sigma_c^a \sigma_t^b$, where $a, b = 0, \dots, 3$ and the subscripts c and t denote the control and target qubits, respectively. After applying the CZ unitary $\Lambda = |0\rangle\langle 0|_c \otimes \mathbb{I}_t + |1\rangle\langle 1|_c \otimes Z_t$ [91], we apply Pauli operators $\sigma_c^c \sigma_t^d$ such that $\sigma_c^c \sigma_t^d = \Lambda \sigma_c^a \sigma_t^b \Lambda^\dagger$. Following Ref. [92], this is given by $c = a + b(3 - b)(3 - 2a)/2$, $d = b + a(3 - a)(3 - 2b)/2$. This noise tailoring makes the errors more well-behaved and better suited for error mitigation techniques such as zero-noise extrapolation (ZNE) [92–94]. A schematic circuit for the HVA with 1 layer on an 8-qubit sub-lattice is shown in Fig. 3. The twirling operation is depicted in Fig. 4.

The variational optimization in the HVA is first performed on a classical simulator, and the circuits are then run on the QPU for the optimal choice of parameters. While this approach circumvents the hybrid quantum/classical computation, it nevertheless serves as a benchmark for how well the quantum processor performs in proof-of-concept experiments. For comparison, recent state of the art results for many body Hamiltonian simulations have either opted for purely classical optimization instead of a VQE step [95], or running their algorithms

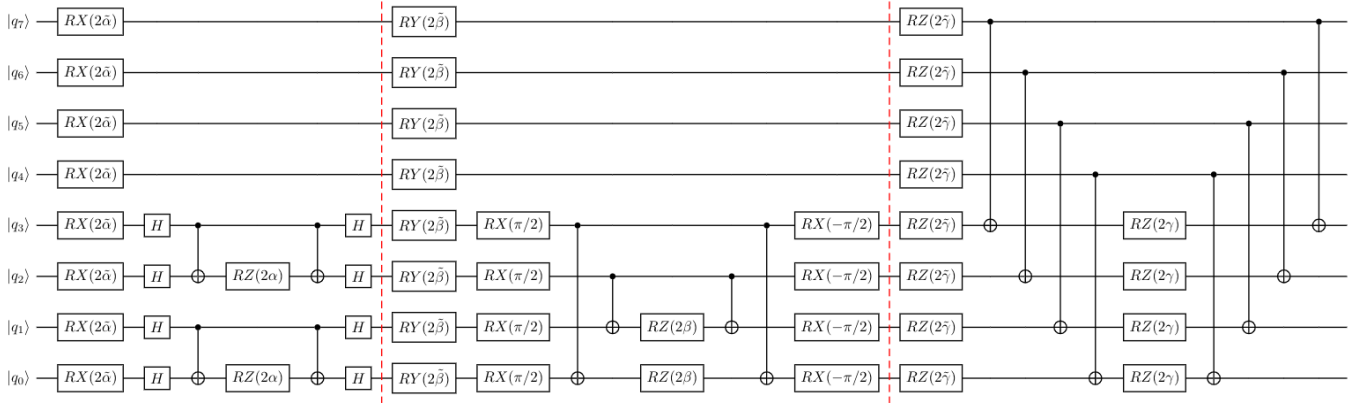


FIG. 3. **HVA with 1 layer on 8-qubits.** The Hamiltonian Variational Ansatz (HVA) with 1 layer on 8 qubits, split into commuting blocks. The first block corresponds to the operation $e^{-i\tilde{\alpha}\sum_q X_q} e^{-i\alpha\sum_{(i,j)\in X\text{-links}} X_i X_j}$, the second to $e^{-i\tilde{\beta}\sum_q Y_q} e^{-i\beta\sum_{(i,j)\in Y\text{-links}} Y_i Y_j}$, and the third to $e^{-i\tilde{\gamma}\sum_q Z_q} e^{-i\gamma\sum_{(i,j)\in Z\text{-links}} Z_i Z_j}$. For the circuit shown here, we used $X\text{-links} = \{(q_0, q_1), (q_2, q_3)\}$, $Y\text{-links} = \{(q_0, q_3), (q_1, q_2)\}$, and $Z\text{-links} = \{(q_0, q_4), (q_1, q_5), (q_2, q_6), (q_3, q_7)\}$.

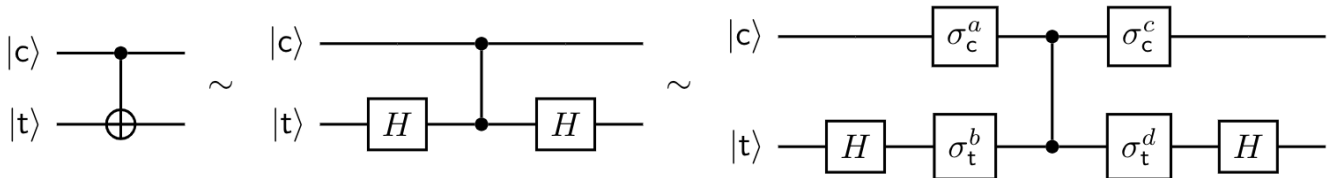


FIG. 4. **Twirled CZ used to compile a CNOT.** Every use of the CNOT gate in Fig. 3 is compiled to a native CZ with some single-qubit gates. Assuming that the major source of noise lies in the 2-qubit gates, we apply random Pauli operators before every use of the CZ, and then apply another pair of Pauli operators in order to twirl the noise channel associated with the CZ into a stochastic Pauli channel. The relationship between the indices $a, b, c, d \in \{0, 1, 2, 3\}$ (denoting respectively the Pauli operators $\{\mathbb{I}, X, Y, Z\}$) is given in III D. All three circuits depicted above are logically equivalent, but generally lead to different noise characteristics.

on smaller numbers of qubits [18, 96].

We perform digital ZNE by first exaggerating the errors in the circuit by replacing a subset of CZs by an odd multiple of them. We choose such subsets to increase the total CZ count in the circuit by a factor of $\lambda = 1, 1.5, 2, 3, 5$. For each scale factor λ , we run 100 different twirled circuits for 1000 shots each. For $\lambda = 1$, we have a total of 16 CZs, 2 for each of the edges. For $\lambda = 1.5$, we run 25 different twirled circuits for each of the scenarios where we replace (a) every CZ in the XX-links with 3 CZs, (b) every CZ in the YY-links with 3 CZs, (c) every CZ in two of the four ZZ-links with 3 CZs, and (d) every CZ in the remaining two of the four ZZ-links with 3 CZs. For $\lambda = 2$, we run 50 different twirled circuits for each of the scenarios where we replace (i) every CZ in the XX- and YY-links with 3 CZs, and (ii) every CZ in the ZZ-links with 3 CZs. For $\lambda = 3$ ($\lambda = 5$), we simply take 100 different twirled circuits where we replace every CZ in the circuit with 3 (5) CZs.

For each of the 100 twirled circuits in each scale factor family, we estimate the cost function (2.3). Each of these expectation value estimates are mitigated for readout errors. This is done by first computing a $2^8 \times 2^8$ confusion matrix of the form $p(\text{read}|\text{prepared})$ obtained

by preparing a bitstring, then computing the fraction of each of 2^8 bitstrings from 10,000 shots to estimate the conditional probabilities, then repeating this procedure for all 2^8 bitstrings. By inverting this confusion matrix, and multiplying this by the vector of empirical probabilities of bitstrings, we obtain a readout error mitigated estimate of the probability of outcomes of all bitstrings. In turn, these lead to readout-error-mitigated estimates of the cost function (2.3) in each of the 100 circuits for any given family associated with a scale factor. We then average these expectation values over all 100 circuits to produce a single value representing the family of circuits associated with a given scale factor. These representative values are then plotted against the scale factors, and a polynomial fit is found to extrapolate to the $\lambda = 0$ (zero noise) limit to obtain an estimate of the cost function mitigated for both gate and readout errors.

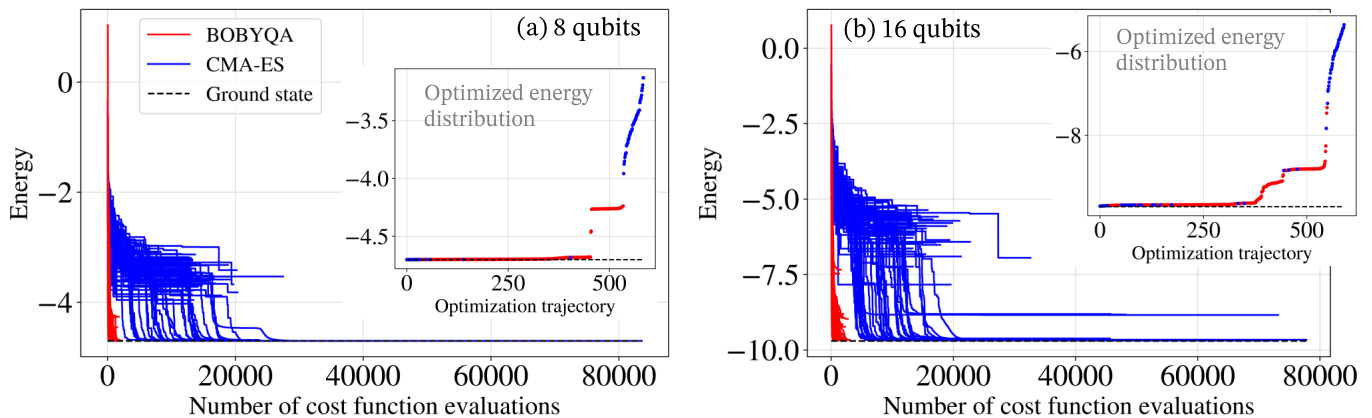


FIG. 5. **Noiseless optimization with BOBYQA and CMA-ES.** The cost function associated with the 4-layer HVA and the parameter set (GL + h) is optimized by BOBYQA (red) with 501 random initial values and CMA-ES (blue) with 80 random initial values. For both (a) 8 qubits and (b) 16 qubits, BOBYQA converges faster than CMA-ES. The optimized energy distribution (see insets) shows that the solutions of CMA-ES give overall better results but are also less consistent. The mixed usage of the two optimizers provides a complementary cross-check of each other result.

IV. RESULTS

A. Statevector simulations

We test the optimizers listed in Table II using the cost function (2.3) associated with the four-layer HVA for the 8-qubit and 16-qubit lattices shown in Fig. 1 and the parameter choice (GL + h) in Table I. This cost function has 24 parameters to be optimized. The results using a statevector simulator are summarized in Table III.

BFGS and BOBYQA are susceptible to local extrema and their performance highly depends on the initial choice of the parameters. We employ a multiple-initial-condition strategy and randomly pick 501 initial parameter values to start with. In general, the number of initial values required for a good result will increase with the number of parameters of the cost function. BOBYQA gives a smaller error in energy compared to BFGS in both 8-qubit and 16-qubit tests, and BOBYQA also converges much faster than BFGS, which requires the costly computation of gradients by finite-difference methods. The other local optimizer, SPSA, is less susceptible to local extrema due to its stochastic nature. However, its convergence is slow and will require many iterations in order to achieve good accuracy. Among the local optimizers, BOBYQA with multiple initial values gives the best performance in terms of both the accuracy of the result and the speed of convergence.

CMA-ES and dual annealing are non-local optimizers that are able to escape from local extrema. Table III shows that both optimizers converge toward a minimum with energy close to the exact value even starting from just one initial value. CMA-ES consistently converges faster among the two. Obtaining the best performance from CMA-ES requires fine tuning of the optimizer meta-parameters, which depends on the neighborhood of the initial value and is challenging to determine *a priori*. To

avoid becoming overly sensitive to the choice of meta-parameters, we also employ a multiple-initial-value strategy with 80 random initial values. For our VQE application, the CMA-ES optimization with multiple initial values consistently shows improvement over that with a single initial value.

To benchmark different ansatzes, we employ both BOBYQA with 501 random initial values and CMA-ES with 80 random initial values and report the better result from the two methods. Different ansatzes (and different layer numbers) result in vastly different cost-function landscapes and numbers of parameters. A mixed usage of different optimization algorithms, which is widely used in black-box optimization, helps us better navigate through the vast varieties of cost functions. In Fig. 5, we study the noiseless optimization for each optimizer with different initial values. For both 8-qubit and 16-qubit cases, CMA-ES needs more cost function evaluations to converge, as expected for a non-local optimizer. As indicated by the optimized energy distribution shown in the insets of Fig. 5, some optimization runs with CMA-ES give the best result but others can be far off. The runs also converge to different optimized parameters with the two different optimizers and also different initial values. This makes the inclusion of the BOBYQA results helpful, since it allows us to crosscheck the optimizations. We expect that VQE optimization carried out on QPUs will also benefit from this approach of mixed optimizers with multiple initial values, especially when the QPU's clock rate becomes sufficiently high to support a large number of cost function evaluations.

We apply this mixed optimization approach to optimize the three different ansatzes (HVA, HEA-CZ, HEA-XY) with different numbers of layers using a statevector simulator. To make our observation more representative, we run the optimization test with three different setups, namely 8-qubit (GL+ h), 16-qubit (GL+ h) and 8-qubit

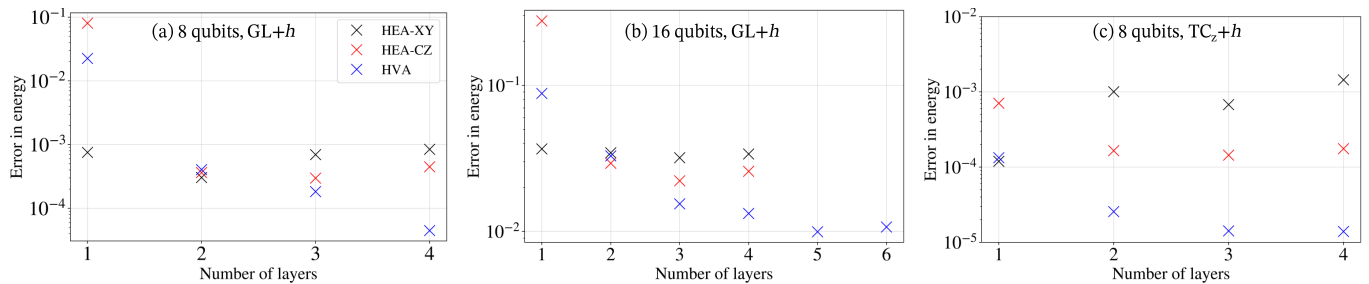


FIG. 6. **Ansatz benchmark by statevector simulation.** The three different ansatzes are optimized with respect to three different setups, (a) 8-qubit lattice with $(GL+h)$, (b) 16-qubit lattice with $(GL+h)$ and (c) 8-qubit lattice with (TC_z+h) . The HEA-CZ (red crosses) and the HEA-XY (black crosses) show a bigger error in energy compared to that of the HVA (blue crosses). This performance difference is mainly due to the difficulty in optimizing the two HEAs with a large number of parameters, as suggested by the minimal improvement of the error when increasing the number of layers of the HEAs.

TABLE III. **Optimizer performance with statevector simulator.** We test the optimizers with 8 qubits and 16 qubits using a four-layer HVA and the $(GL+h)$ parameter set. We employ a multiple-initial-value strategy to BFGS and BOBYQA to avoid the local optimizers being trapped at a bad local extreme. The lowest energy is reported for the multiple-initial-values strategy. While the genetic algorithm (CMA-ES) is less susceptible to local extrema, a multiple-initial-values strategy with a smaller iteration cutoff also improves its performance. SPSA and dual annealing converge slowly and reach the maximum iteration (cutoff). Note that the error in energy is the difference between the optimized energy and the ground-state energy computed by ED.

Qubits	Optimizer	Error in energy	Cost function evaluations
8	BFGS 501 initial values	0.00094	mean: 5352 max: 10865
16	BFGS 501 initial values	0.02672	mean: 5569 max: 10186
8	BOBYQA 501 initial values	0.00045	mean: 1099 max: 1920
16	BOBYQA 501 initial values	0.01744	mean: 1255 max: 3049
8	CMA-ES	0.00015	43290
16	CMA-ES	0.04036	49335
8	CMA-ES 80 initial values	0.00005	mean: 20528 max: 83590
16	CMA-ES 80 initial values	0.01327	mean: 27504 max: 73138
8	Dual annealing	0.00252	100000 (cutoff)
16	Dual annealing	0.04634	100106 (cutoff)
8	SPSA	0.04500	100000 (cutoff)
16	SPSA	0.08145	100000 (cutoff)

(TC_z+h) (see Table I for the parameters values). The results in Fig. 6 show that the HVA in general outperforms the other two HEAs when a deeper ansatz is used to re-

duce the error in energy. However, this behavior should not be interpreted as implying the superiority of the HVA as compared to the two HEAs. The main reason for the HEAs' worse performance is rather due to the extreme difficulty in the optimization, which is directly related to the barren plateau phenomenon [23]. The number of parameters increases rapidly for HEAs; for example, the 4-layer HEA-XY for 16 qubits has 536 parameters. This makes it excessively challenging to scale up the VQE with HEAs to a longer circuit depth or a larger system size. This is also revealed by the fact that two HEAs show nearly no improvement with increasing number of layers in Fig. 6. Hence, the VQE using HVA will be a more promising approach toward quantum advantage for the square-octagon-lattice Kitaev model.

B. QPU experiment

The experimental method has been described in Sec. III D. As discussed there, we perform a proof-of-concept experiment using the HVA with 1 layer on an 8-qubit sub-lattice of Aspen-9 consisting of qubits (10, 11, 12, 13, 24, 25, 26, 27), see Fig. 1(b). A schematic HVA-1 circuit is depicted in Fig. 3, and in order to execute this on Aspen-9, we identify qubits $(q_0, q_1, q_2, q_3, q_4, q_5, q_6, q_7)$ with respectively qubits (12, 25, 26, 11, 13, 24, 27, 10) on Aspen-9. To perform digital zero noise extrapolation (ZNE), we increase the total CZ count in the circuit by various scale factors, and also twirl them with random Pauli operators to tailor the noise into a stochastic channel, which may allow ZNE to work better. The expectation values measured at each scale factor are also mitigated for readout errors. Fig. 7 plots the Hamiltonian expectation values in the classically-optimized variational state for various scale factors, and a best-fit line for the first three scale factors. (The final two scale factors are omitted from the fit because the noise in the system overwhelms any meaningful patterns one could exploit in the extrapolation scheme beyond a scale factor of 2.) Using the best-fit line, we

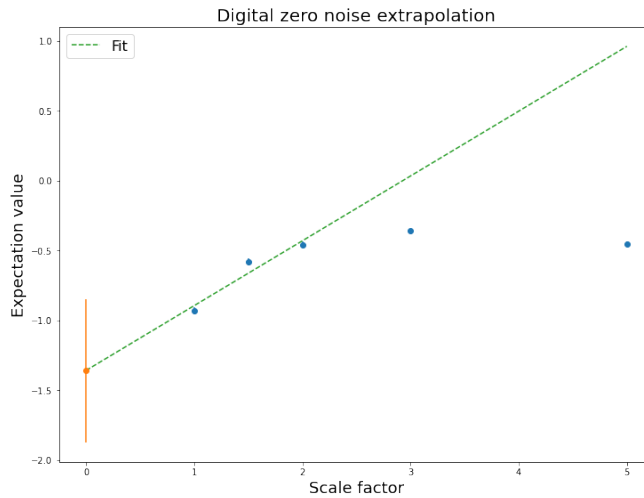


FIG. 7. Digital ZNE on Pauli twirled, readout error mitigated circuits. The x -axis represents the scale by which the total CZ count in the circuit is increased by. A line of best fit is obtained for the first three sets of data points. The data points corresponding to scale factor being 3 and 5 are dominated by noise and are not used for ZNE. The standard error in each of the average expectation values over all twirled circuits at the various scale factors is $O(1/\sqrt{100,000})$, and negligibly small at the scale of this plot. The Hamiltonian expectation value, plotted on the y -axis, is then extrapolated back to the $x = 0$ limit to obtain a noiseless estimate with the depicted error.

find an extrapolated value for the expectation value to be ~ -1.36 (with a standard deviation of ~ 0.51), which is closer to the best value of ~ -4.23 that the one-layer HVA can produce than if the error mitigation techniques described previously were not used. Although this is a proof-of-concept experiment, it motivates the use of sophisticated error mitigation techniques along with better gate fidelities to achieve better results on the QPU in the future.

V. CONCLUSION

In this work, we investigated and benchmarked the appropriate ansatzes and optimization strategies to find the ground state of the square-octagon-lattice Kitaev model with a VQE approach. We showed that the HVA generally outperforms the two HEAs using CZ or XY gates in the entangling layers. The HEAs require an expensive optimization process due to their rapidly increasing number of parameters with system size and circuit depth, and the unstructured nature of HEAs also makes them susceptible to barren plateaus. The HVA is associated with a relatively easy optimization and is thus better suited to the QPU experiments. We conducted an experimental test to run a classically optimized 8-qubit HVA circuit on the Aspen-9 QPU. The result shows a noticeable difference from the statevector simulation after performing randomized compilation, readout error mitigation and zero-noise extrapolation to mitigate the errors. This suggests that extra error mitigation techniques and performing the VQE optimization directly on the QPU would be required to extract useful results from the QPU

for the future implementation of Kitaev-model VQE experiments.

Multiple optimization algorithms have been tested to optimize the cost function associated with our VQE application. We find that a mixed usage of different optimizers with multiple initial values gives a much more consistent and better result than just using one specific optimizer with one initial value. In particular, a local optimizer (BOBYQA) mixed with a non-local optimizer (CMA-ES) is shown to be an appropriate strategy for VQE calculations of the Kitaev model. Although we performed our tests with the noiseless simulator, we expect that QPU experiments will also benefit from this approach as long as the QPU's clock rate is high enough to support the required number of cost function evaluations.

ACKNOWLEDGMENTS

This material is based upon work supported by the U.S. Department of Energy, Office of Science, National Quantum Information Science Research Centers, Superconducting Quantum Materials and Systems Center (SQMS) under the contract No. DE-AC02-07CH11359. We would like to thank the entire SQMS algorithms team for fruitful and thought provoking discussions around these works. We would also like to thank the Rigetti team for assistance with running experiments on the Aspen-9 processor, particularly Matt Reagor, Mark Hodson, Bram Evert, Alex Hill, Eric Hulburd and Dylan Anthony. P.P.O. acknowledges useful discussions with Alexander Huynh and Anirban Mukherjee. Some calculations were

performed as part of the XSEDE computational Project

No. TG-MCA93S030 on Bridges-2 at the Pittsburgh supercomputer center.

-
- [1] A. M. Childs, D. Maslov, Y. Nam, N. J. Ross, and Y. Su, *Proceedings of the National Academy of Sciences* **115**, 9456 (2018), <https://www.pnas.org/content/115/38/9456.full.pdf>.
- [2] P. W. Shor, *Phys. Rev. A* **52**, R2493 (1995).
- [3] J. Roffe, *Contemporary Physics* **60**, 226 (2019), <https://doi.org/10.1080/00107514.2019.1667078>.
- [4] F. Arute, K. Arya, R. Babbush, D. Bacon, J. C. Bardin, R. Barends, A. Bengtsson, S. Boixo, M. Broughton, B. B. Buckley, D. A. Buell, B. Burkett, N. Bushnell, Y. Chen, Z. Chen, Y.-A. Chen, B. Chiaro, R. Collins, S. J. Cotton, W. Courtney, S. Demura, A. Derk, A. Dunsworth, D. Eppens, T. Eickl, C. Erickson, E. Farhi, A. Fowler, B. Foxen, C. Gidney, M. Giustina, R. Graff, J. A. Gross, S. Habegger, M. P. Harrigan, A. Ho, S. Hong, T. Huang, W. Huggins, L. B. Ioffe, S. V. Isakov, E. Jeffrey, Z. Jiang, C. Jones, D. Kafri, K. Kechedzhi, J. Kelly, S. Kim, P. V. Klimov, A. N. Korotkov, F. Kostritsa, D. Landhuis, P. Laptev, M. Lindmark, E. Lucero, M. Marthaler, O. Martin, J. M. Martinis, A. Maruszczyk, S. McArdle, J. R. McClean, T. McCourt, M. McEwen, A. Megrant, C. Mejuto-Zaera, X. Mi, M. Mohseni, W. Mruczkiewicz, J. Mutus, O. Naaman, M. Neeley, C. Neill, H. Neven, M. Newman, M. Yuezhen Niu, T. E. O'Brien, E. Ostby, B. Pató, A. Petukhov, H. Putterman, C. Quintana, J.-M. Reiner, P. Roushan, N. C. Rubin, D. Sank, K. J. Satzinger, V. Smelyanskiy, D. Strain, K. J. Sung, P. Schmitteckert, M. Szalay, N. M. Tubman, A. Vainsencher, T. White, N. Vogt, Z. J. Yao, P. Yeh, A. Zalcman, and S. Zanker, arXiv e-prints , arXiv:2010.07965 (2020), [arXiv:2010.07965](https://arxiv.org/abs/2010.07965) [quant-ph].
- [5] A. Kitaev, *Annals of Physics* **321**, 2–111 (2006).
- [6] S. Yang, D. L. Zhou, and C. P. Sun, *Phys. Rev. B* **76**, 180404 (2007).
- [7] J. Preskill, *Quantum* **2**, 79 (2018).
- [8] M. Cerezo, A. Arrasmith, R. Babbush, S. C. Benjamin, S. Endo, K. Fujii, J. R. McClean, K. Mitarai, X. Yuan, L. Cincio, and P. J. Coles, Variational quantum algorithms (2020), [arXiv:2012.09265](https://arxiv.org/abs/2012.09265) [quant-ph].
- [9] K. Bharti, A. Cervera-Liarta, T. H. Kyaw, T. Haug, S. Alperin-Lea, A. Anand, M. Degroote, H. Heimonen, J. S. Kottmann, T. Menke, W.-K. Mok, S. Sim, L.-C. Kwek, and A. Aspuru-Guzik, Noisy intermediate-scale quantum (nisq) algorithms (2021), [arXiv:2101.08448](https://arxiv.org/abs/2101.08448) [quant-ph].
- [10] A. Peruzzo, J. McClean, P. Shadbolt, M.-H. Yung, X.-Q. Zhou, P. J. Love, A. Aspuru-Guzik, and J. L. O'Brien, *Nat. Comm.* **5**, 1 (2014).
- [11] P. J. J. O'Malley *et al.*, *Phys. Rev. X* **6**, 031007 (2016).
- [12] J. R. McClean, J. Romero, R. Babbush, and A. Aspuru-Guzik, *New Journal of Physics* **18**, 023023 (2016), [arXiv:1509.04279](https://arxiv.org/abs/1509.04279) [quant-ph].
- [13] A. Kandala, A. Mezzacapo, K. Temme, M. Takita, M. Brink, J. M. Chow, and J. M. Gambetta, *Nature* **549**, 242 (2017).
- [14] H. R. Grimsley, S. E. Economou, E. Barnes, and N. J. Mayhall, *Nature Communications* **10**, 3007 (2019), [arXiv:1812.11173](https://arxiv.org/abs/1812.11173) [quant-ph].
- [15] W. J. Huggins, J. Lee, U. Baek, B. O'Gorman, and K. B. Whaley, *New Journal of Physics* **22**, 073009 (2020), [arXiv:1909.09114](https://arxiv.org/abs/1909.09114) [quant-ph].
- [16] H. L. Tang, V. O. Shkolnikov, G. S. Barron, H. R. Grimsley, N. J. Mayhall, E. Barnes, and S. E. Economou, *PRX Quantum* **2**, 020310 (2021), [arXiv:1911.10205](https://arxiv.org/abs/1911.10205) [quant-ph].
- [17] O. Romesh Meitei, B. T. Gard, G. S. Barron, D. P. Pappas, S. E. Economou, E. Barnes, and N. J. Mayhall, arXiv e-prints , arXiv:2008.04302 (2020), [arXiv:2008.04302](https://arxiv.org/abs/2008.04302) [quant-ph].
- [18] Y. Zhang, L. Cincio, C. F. A. Negre, P. Czarnik, P. Coles, P. M. Anisimov, S. M. Mniszewski, S. Tretiak, and P. A. Dub, arXiv e-prints , arXiv:2106.07619 (2021), [arXiv:2106.07619](https://arxiv.org/abs/2106.07619) [quant-ph].
- [19] D. Wecker, M. B. Hastings, and M. Troyer, *Phys. Rev. A* **92**, 042303 (2015).
- [20] E. Farhi, J. Goldstone, S. Gutmann, and M. Sipser, arXiv preprint quant-ph/0001106 (2000).
- [21] E. Farhi, J. Goldstone, and S. Gutmann, A quantum approximate optimization algorithm (2014), [arXiv:1411.4028](https://arxiv.org/abs/1411.4028) [quant-ph].
- [22] R. Wiersema, C. Zhou, Y. de Sereville, J. F. Carrasquilla, Y. B. Kim, and H. Yuen, *PRX Quantum* **1**, 020319 (2020).
- [23] J. R. McClean, S. Boixo, V. N. Smelyanskiy, R. Babbush, and H. Neven, *Nat. Commun.* **9**, 4812 (2018).
- [24] M. Larocca, P. Czarnik, K. Sharma, G. Muraleedharan, P. J. Coles, and M. Cerezo, Diagnosing barren plateaus with tools from quantum optimal control (2021), [arXiv:2105.14377](https://arxiv.org/abs/2105.14377) [quant-ph].
- [25] M. Hermanns, I. Kimchi, and J. Knolle, Annual Review of Condensed Matter Physics **9**, 17 (2018).
- [26] H. Takagi, T. Takayama, G. Jackeli, G. Khaliullin, and S. E. Nagler, *Nature Reviews Physics* **1**, 264 (2019).
- [27] C. Hickey and S. Trebst, *Nature Communications* **10**, 530 (2019).
- [28] C. Nayak, S. H. Simon, A. Stern, M. Freedman, and S. Das Sarma, *Reviews of Modern Physics* **80**, 1083–1159 (2008).
- [29] Y.-C. Lee, C. G. Brell, and S. T. Flammia, *Journal of Statistical Mechanics: Theory and Experiment* **2017**, 083106 (2017).
- [30] M. H. Freedman, M. Larsen, and Z. Wang, *Communications in Mathematical Physics* **227**, 605 (2002).
- [31] G. Jackeli and G. Khaliullin, *Phys. Rev. Lett.* **102**, 017205 (2009).
- [32] A. Banerjee, C. A. Bridges, J.-Q. Yan, A. A. Aczel, L. Li, M. B. Stone, G. E. Granroth, M. D. Lumsden, Y. Yiu, J. Knolle, and et al., *Nature Materials* **15**, 733–740 (2016).
- [33] A. Banerjee, P. Lampen-Kelley, J. Knolle, C. Balz, A. A. Aczel, B. Winn, Y. Liu, D. Pajerowski, J. Yan, C. A. Bridges, and et al., *npj Quantum Materials* **3**, 8 (2018).
- [34] Y. Kasahara, K. Sugii, T. Ohnishi, M. Shimozawa, M. Yamashita, N. Kurita, H. Tanaka, J. Nasu, Y. Motome, T. Shibauchi, *et al.*, *Physical review letters* **120**,

- 217205 (2018).
- [35] T. Yokoi, S. Ma, Y. Kasahara, S. Kasahara, T. Shibauchi, N. Kurita, H. Tanaka, J. Nasu, Y. Motome, C. Hickey, *et al.*, arXiv preprint arXiv:2001.01899 (2020).
- [36] J. Chaloupka, G. Jackeli, and G. Khaliullin, *Phys. Rev. Lett.* **105**, 027204 (2010).
- [37] H.-C. Jiang, Z.-C. Gu, X.-L. Qi, and S. Trebst, *Phys. Rev. B* **83**, 245104 (2011).
- [38] J. Chaloupka, G. Jackeli, and G. Khaliullin, *Phys. Rev. Lett.* **110**, 097204 (2013).
- [39] J. Osorio Iregui, P. Corboz, and M. Troyer, *Phys. Rev. B* **90**, 195102 (2014).
- [40] J. G. Rau, E. K.-H. Lee, and H.-Y. Kee, *Phys. Rev. Lett.* **112**, 077204 (2014).
- [41] K. Shinjo, S. Sota, and T. Tohyama, *Phys. Rev. B* **91**, 054401 (2015).
- [42] S. M. Winter, Y. Li, H. O. Jeschke, and R. Valentí, *Phys. Rev. B* **93**, 214431 (2016).
- [43] R. Yadav, N. A. Bogdanov, V. M. Katukuri, S. Nishimoto, J. Van Den Brink, and L. Hozoi, *Scientific reports* **6**, 1 (2016).
- [44] M. Gohlke, R. Verresen, R. Moessner, and F. Pollmann, *Phys. Rev. Lett.* **119**, 157203 (2017).
- [45] D. Gotfryd, J. Rusnačko, K. Wohlfeld, G. Jackeli, J. c. v. Chaloupka, and A. M. Oleś, *Phys. Rev. B* **95**, 024426 (2017).
- [46] Z. Zhu, I. Kimchi, D. N. Sheng, and L. Fu, *Phys. Rev. B* **97**, 241110 (2018).
- [47] N. D. Patel and N. Trivedi, *Proceedings of the National Academy of Sciences* **116**, 12199 (2019).
- [48] J. S. Gordon, A. Catuneanu, E. S. Sørensen, and H.-Y. Kee, *Nature communications* **10**, 1 (2019).
- [49] P. Czarnik, A. Francuz, and J. Dziarmaga, *Physical Review B* **100**, 165147 (2019).
- [50] H.-Y. Lee, R. Kaneko, L. E. Chern, T. Okubo, Y. Yamaji, N. Kawashima, and Y. B. Kim, *Nature communications* **11**, 1 (2020).
- [51] S. R. White, *Phys. Rev. Lett.* **69**, 2863 (1992).
- [52] U. Schollwöck, *Annals of Physics* **326**, 96–192 (2011).
- [53] M. Fishman, S. R. White, and E. Miles Stoudenmire, arXiv e-prints , arXiv:2007.14822 (2020), arXiv:2007.14822 [cs.MS].
- [54] P. A. Mishchenko, Y. Kato, and Y. Motome, arXiv e-prints , arXiv:2106.07937 (2021), arXiv:2106.07937 [cond-mat.str-el].
- [55] M. Kurita, Y. Yamaji, S. Morita, and M. Imada, *Physical Review B* **92**, 10.1103/physrevb.92.035122 (2015).
- [56] G. Kells, J. Kailasvuori, J. K. Slingerland, and J. Vala, *New Journal of Physics* **13**, 095014 (2011).
- [57] S. S. Hong, A. T. Papageorge, P. Sivarajah, G. Crossman, N. Didier, A. M. Polloreno, E. A. Sete, S. W. Turkowski, M. P. da Silva, and B. R. Johnson, *Phys. Rev. A* **101**, 012302 (2020).
- [58] D. M. Abrams, N. Didier, M. P. Johnson, Blake R. da Silva, and C. A. Ryan, *Nature Electronics* **3**, 744 (2020).
- [59] M. Reagor *et al.*, *Sci. Adv.* **4**, eaao3603 (2018).
- [60] C. Berke, S. Trebst, and C. Hickey, *Phys. Rev. B* **101**, 214442 (2020).
- [61] C. Hickey, M. Gohlke, C. Berke, and S. Trebst, *Phys. Rev. B* **103**, 064417 (2021).
- [62] M. G. Yamada, *Phys. Rev. Research* **3**, L012001 (2021).
- [63] A. Kitaev, *Annals of Physics* **303**, 2–30 (2003).
- [64] X.-G. Wen, *Phys. Rev. Lett.* **90**, 016803 (2003).
- [65] Z. Nussinov and G. Ortiz, *Annals of Physics* **324**, 977–1057 (2009).
- [66] B. J. Brown, W. Son, C. V. Kraus, R. Fazio, and V. Vedral, *New Journal of Physics* **13**, 065010 (2011).
- [67] D.-B. Zhang, Z.-H. Yuan, and T. Yin, (2020), arXiv:2006.15781 [quant-ph].
- [68] F. Zhang, N. Gomes, Y. Yao, P. P. Orth, and T. Iadecola, arXiv e-prints , arXiv:2104.12636 (2021), arXiv:2104.12636 [quant-ph].
- [69] K. M. Nakanishi, K. Mitarai, and K. Fujii, *Phys. Rev. Research* **1**, 033062 (2019).
- [70] O. Higgott, D. Wang, and S. Brierley, *Quantum* **3**, 156 (2019).
- [71] A. Gu, A. Lowe, P. A. Dub, P. J. Coles, and A. Arrasmith, arXiv e-prints , arXiv:2108.10434 (2021), arXiv:2108.10434 [quant-ph].
- [72] W. W. Ho and T. H. Hsieh, *SciPost Phys.* **6**, 29 (2019).
- [73] C. Cade, L. Mineh, A. Montanaro, and S. Stanisic, *Phys. Rev. B* **102**, 235122 (2020).
- [74] W. Lavrijsen, A. Tudor, J. Müller, C. Iancu, and W. de Jong, in *2020 IEEE International Conference on Quantum Computing and Engineering (QCE)* (2020) pp. 267–277.
- [75] A. Anand, M. Degroote, and A. Aspuru-Guzik, *Machine Learning: Science and Technology* **2**, 045012 (2021).
- [76] A. W. Harrow and J. C. Napp, *Phys. Rev. Lett.* **126**, 140502 (2021).
- [77] V. Havlíček, A. D. Córcoles, K. Temme, A. W. Harrow, A. Kandala, J. M. Chow, and J. M. Gambetta, *Nature* **567**, 209 (2019).
- [78] E. Peters, J. Caldeira, A. Ho, S. Leichenauer, M. Mohseni, H. Neven, P. Spentzouris, D. Strain, and G. N. Perdue, *Machine learning of high dimensional data on a noisy quantum processor* (2021), arXiv:2101.09581 [quant-ph].
- [79] R. S. Smith, M. J. Curtis, and W. J. Zeng, arXiv e-prints , arXiv:1608.03355 (2016), arXiv:1608.03355 [quant-ph].
- [80] R. S. Smith, E. C. Peterson, M. G. Skilbeck, and E. J. Davis, *Quantum Science and Technology* **5**, 044001 (2020), arXiv:2003.13961 [quant-ph].
- [81] P. J. Karalekas, N. A. Tezak, E. C. Peterson, C. A. Ryan, M. P. da Silva, and R. S. Smith, *Quantum Science and Technology* **5**, 024003 (2020).
- [82] M. J. D. Powell, *Cambridge NA Report NA2009/06* , 26 (2009).
- [83] N. Hansen and A. Ostermeier, *Evol. Comput.* **9**, 159 (2001).
- [84] Y. Xiang, D. Sun, W. Fan, and X. Gong, *Physics Letters A* **233**, 216 (1997).
- [85] J. C. Spall, *IEEE Trans. Automat. Contr.* **37**, 332 (1992).
- [86] L. M. Rios and N. V. Sahinidis, *J. Global Optim.* **56**, 1247 (2013).
- [87] J. Romero, R. Babbush, J. R. McClean, C. Hempel, P. J. Love, and A. Aspuru-Guzik, *Quantum Science and Technology* **4**, 014008 (2018).
- [88] A. Gilyén, S. Arunachalam, and N. Wiebe, *Optimizing quantum optimization algorithms via faster quantum gradient computation*, in *Proceedings of the 2019 Annual ACM-SIAM Symposium on Discrete Algorithms (SODA)* (2019) pp. 1425–1444, <https://epubs.siam.org/doi/pdf/10.1137/1.9781611975482.87>.
- [89] K. Mitarai, Y. O. Nakagawa, and W. Mizukami, *Phys. Rev. Research* **2**, 013129 (2020).
- [90] J. J. Wallman and J. Emerson, *Phys. Rev. A* **94**, 052325

- (2016).
- [91] Note that the same unitary can also be written $\mathbb{I}_c \otimes |0\rangle\langle 0|_t + \mathbb{Z}_c \otimes |1\rangle\langle 1|_t$, so that the CZ gate remains invariant if we swap the labels c and t. It therefore doesn't matter how we assign the labels control/target to the two qubits participating in this interaction.
- [92] Y. Li and S. C. Benjamin, *Phys. Rev. X* **7**, 021050 (2017).
- [93] K. Temme, S. Bravyi, and J. M. Gambetta, *Phys. Rev. Lett.* **119**, 180509 (2017).
- [94] T. Giurgica-Tiron, Y. Hindy, R. LaRose, A. Mari, and W. J. Zeng, in *2020 IEEE International Conference on Quantum Computing and Engineering (QCE)* (2020) pp. 306–316.
- [95] W. J. Huggins, B. A. O’Gorman, N. C. Rubin, D. R. Reichman, R. Babbush, and J. Lee, arXiv e-prints , arXiv:2106.16235 (2021), [arXiv:2106.16235 \[quant-ph\]](#).
- [96] K. Klymko, C. Mejuto-Zaera, S. J. Cotton, F. Wudarski, M. Urbanek, D. Hait, M. Head-Gordon, K. B. Whaley, J. Moussa, N. Wiebe, W. A. de Jong, and N. M. Tubman, arXiv e-prints , arXiv:2103.08563 (2021), [arXiv:2103.08563 \[quant-ph\]](#).